



High efficiency light trapping scheme used for ultrathin c-Si solar cells

Xiaodong Lu*, Yukuo Li, Shuxian Lun, Xinxin Wang, Jie Gao, Yang Wang, Yufeng Zhang

College of New Energy, Bohai University, Jinzhou, Liaoning, 121000, China

ARTICLE INFO

Keywords:

Solar cell
Light trapping
High efficiency

ABSTRACT

Ultrathin c-Si solar cells with their active layer thicknesses ranging from a few micrometers to several tens of micrometers will play a very important role in reducing the material costs of industrial c-Si solar cells. This work presents a new high efficiency light trapping scheme (HE-LTS) with two cavities for ultrathin c-Si solar cells. By analyzing the variations of the important optical parameters of each light trapping unit with its geometric parameters, the light trapping performances of the HE-LTS have been optimized. The results show that the light trapping abilities of the HE-LTS can exceed obviously that of Lambertian LTS in a broad range of geometric parameters for both TE and TM modes; the photocurrent densities of an ultrathin c-Si solar cell with the optimal HE-LTS can reach 36.65 mA/cm² and 40.47 mA/cm² for the TE and TM modes, respectively.

1. Introduction

The industrial c-Si solar cells (c-Si SCs) with their active layer thicknesses from 180 μm to 200 μm are dominant in photovoltaic market and comparing with thin film SCs, the material costs of industrial c-Si SCs are still higher, so reducing their active layer thicknesses from the current thicknesses to the thicknesses of several tens of micrometers or a few micrometers has become a hot topic in the research field of c-Si SCs [1]. Due to the broader absorption band and indirect band gap nature of c-Si material, the light absorption abilities of the ultrathin c-Si SCs with their active layer thicknesses below 50 μm, which become much worse, have become the main constraint on enhancing the efficiencies of these c-Si SCs [2].

Light trapping schemes (LTSs), which are often micro-/nano-structures fabricated on the front and/or back surfaces of SCs, are the main technique to enhance the light absorption of various SCs, including ultrathin c-Si SCs, over their whole absorption wavelength ranges, especially over their weak absorption wavelength ranges [3]. Until now, many high-efficiency LTSs (HE-LTSs) have been proven to be effective in enhancing the absorption of light for different active layer materials, such as triangular gratings [4], pyramid gratings [5], nanowires [6], nanoholes [7], nanocones [8], photonic crystals [9] and plasmonic nanostructures [10,11]. Generally, the feature sizes of HE-LTSs are on the same orders of the maximum absorption wavelengths of different active layer materials, so their light trapping effects are mainly dependent on diffusion reflection [6–8], scattering [6–8,10,11] or diffractive [4,5] effect. By carefully designing the combination of three effects, HE-LTSs can effectively reduce the reflective loss of the front

surfaces of SCs and extend the optical path length of light within the active layer of SCs.

The strong synergistic effect of a HE-LTS with a specific size, shape and material often occurs at some specific wavelengths, which means the absorption spectrum for a solar cell with a specific HE-LTS always presents a multi-peak curve, where the rapid oscillations in its absorption spectrum are related with the strong and weak synergistic effects of the HE-LTS [4–11]. For example, by using some optimal triangular or pyramid grating structures, the absorptance of an ultrathin c-Si SCs with the active layer thicknesses of a few micrometers can be effective increased in the whole absorption wavelength range, but in the wavelength range from 700 nm to 1100 nm, many narrow absorption peaks appear in the absorption spectrum and their amplitudes will decrease rapidly in function of increasing wavelength [4,5]. The absorption spectra of ultrathin c-Si SCs with other optimal HE-LTSs, such as nanowires, nanoholes, nanocones, photonic crystals and plasmonic nanostructures, will show the same behaviors as those with triangular or pyramid grating structures. Due to the sizes of these HE-LTSs generally smaller than those of triangular or pyramid grating structures, the narrow peaks in the absorption spectra will exhibit obviously variations with increasing wavelength [6–11]. The oscillations in the amplitude of the absorption spectrum will limit the overall synergistic effects of these HE-LTSs especially in the wavelength range near the bandgap of c-Si active layer. Comparing with Lambertian light trapping scheme, which is an ideal random scatter structure on the front and/or back surfaces of a c-Si SC and can enhance the path length of incident light inside c-Si active layer by a factor up to $4n^2$, where n is the index of refraction for c-Si material, the synergistic effects of most of HE-LTSs

* Corresponding author.

E-mail address: lxid2211@sina.com (X. Lu).

<https://doi.org/10.1016/j.solmat.2019.03.036>

Received 4 January 2019; Received in revised form 18 March 2019; Accepted 19 March 2019

Available online 28 March 2019

0927-0248/ © 2019 Elsevier B.V. All rights reserved.

for a specific ultrathin c-Si SC can exceed that of Lambertian light trapping scheme only at some specific wavelengths. In order to exceed Lambertian light trapping scheme in a broad wavelength range and improve the absorption spectrum characteristics of a single HE-LTS, the different combinations of difference HE-LTSs, such as tandem photonic-crystal structure [12], have been proposed, but these schemes often involve more complex process steps and higher precision fabrication.

In our recent work [13], we have proposed a new HE-LTS for ultrathin c-Si SCs, which can reduce greatly the reflection loss of incident light caused by the front-surface electrode and trap light effectively inside the c-Si active layer. By optimizing few geometric parameters of the HE-LTS for TM (transverse magnetic) modes, we have proved that the synergistic effect of the HE-LTS can obviously exceed that of Lambertian light trapping scheme in a broad wavelength range. In this work, considering the difficulties in fabricating the front-surface triangular electrode by conventional printing process, we will replace the front-surface triangular electrode with a flat electrode and provide a complete optimization scheme for the HE-LTS. The light trapping mechanisms and performances of each light trapping unit in the HE-LTS will be evaluated in detail.

2. Ultrathin c-Si SC model and optimization method

Fig. 1(a) shows a typical two dimensional structure of the HE-LTS, which is composed of a semicircle convex (SCL), buffer layer, triangular coupled micro-cavity (TCMC) and resonant optical cavity (ROC). The TCMC is fabricated on the front surface of the c-Si active layer and the ROC is formed by the front and back surface electrodes. The optical connection between the TCMC and buffer layer is established by the coupling hole fabricated on the front surface electrode. The unusual structural units in the HE-LTS, such as the SCL, TCMC, buffer layer and coupling hole, can be easily fabricated by some conventional semiconductor processes [14–16], such as photolithography, wet & dry etching and thin film deposition. In Fig. 1(a), $H1$, $H2$, $H3$, $H4$, $H5$ and $H6$ are the radius of SCL, the heights of buffer layer, front-surface rectangular electrode, TCMC, active layer and back-surface electrode, respectively; $L1$ ($=2 \times H1$), $L2$ and $L3$ are the widths of the repeating unit of the ultrathin c-Si SC, TCMC and coupling hole, respectively. The base angle of the TCMC is denoted by θ_1 . The coordinate system adopted in our discussion is shown in Fig. 1(a), where the origin is defined at the center of the SCL. For convenience, we assume that incident light propagates along the positive Y direction, as shown by Fig. 1(b) θ_{inc} and θ_{lens} denote the incident angle of light incident on the upper surface of the SCL and the deviation angle of light refracted by SCL, respectively. θ_d denotes the deviation angle of light first entering the c-Si active layer.

Fig. 1(b) is the schematic diagram of light trapping process. The light trapping process can be divided into two steps. The first step, which is a process of introducing incident light effectively into the ROC, includes that incident light is first focused by the SCL, then pass through

the buffer layer and finally enter the TCMC. The second step, which is a process of trapping incident light completely inside the ROC, includes that the light entering the TCMC is coupled into the ROC by the stronger refraction and diffraction effects and perfectly trapped inside the ROC. With the aid of the focusing effect of the SCL, the properties of incident light, such as propagation direction and light intensity distribution, will be adjusted to satisfying the requirements of the TCMC for incident light properties. Comparing with other LTSs, the advantages of the HE-LTS include that the reflection losses of incident light caused by the front surface electrode, which account for approximately 10% of the total incident energy, will be effectively decreased; the area of the front-surface electrode can be tremendously increased. The larger area of the front-surface electrode can collect more effectively the photo-generated carriers generated inside the c-Si active layer, which means that those materials with shorter carrier diffusion lengths are also possible to get larger photocurrent densities.

The simulation method used to obtain the reflectance, transmittance, absorbance and photocurrent density can be found in our previous works [3,4,13,17] and the simulation settings, such as boundary conditions and meshing scheme, are the same as those used in Ref. [13]. Because the comprehensive effects of transmission and absorption are more important for a specific trapping unit, here we introduce two types of photocurrent densities to evaluate the light trapping performances of a trapping unit, as following,

$$J_M = \frac{q}{hc} \int_{\lambda} \lambda' M(\lambda') \frac{dI}{d\lambda'} d\lambda' \quad (1)$$

where q , h , c are the charge on an electron, Planck's constant, speed of light, respectively; $dI/d\lambda$ is the power density per unit wavelength of the solar radiation; M , which will be denoted by T or A in different situations, is the photocurrent density calculated by transmittance or absorbance. Considering the common materials used in industrial c-Si SCs, the SCL, buffer layer and TCMC materials are all selected as SiO_2 material and the electrode materials used by the front and back surface are selected as metallic silver. In addition, the refractive indexes of all materials and solar spectrum are from a widely used website of the photovoltaic community [18].

3. Results and discussion

3.1. The focal properties of the SCL

The focal properties of the SCL are the most important criterion for designing and optimizing other parameters of the HE-LTS. In order to obtain the complete intensity distributions of the focal spots for different wavelengths, we first replace the materials of the electrodes, TCMC and c-Si active layer with SiO_2 material and then make the total height of $H2$, $H3$, $H4$, $H5$ and $H6$ large enough. By these setting, incident light refracted by the SCL can display the complete shapes of all

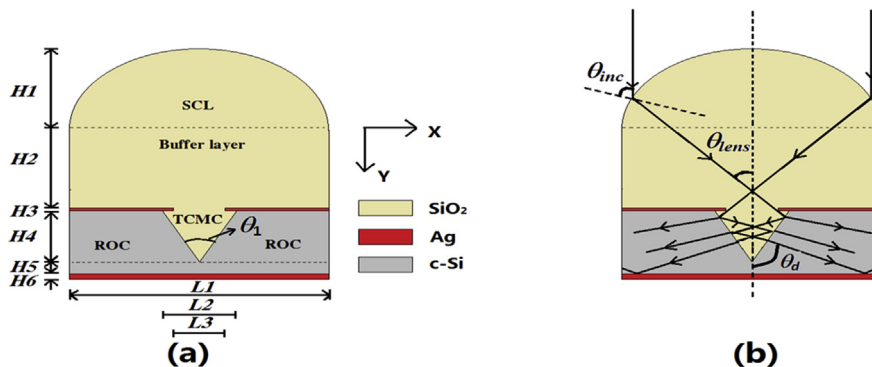


Fig. 1. (a) is a typical structure of ultrathin c-Si SCs with the HE-LTS and (b) is the schematic diagram of light trapping process.

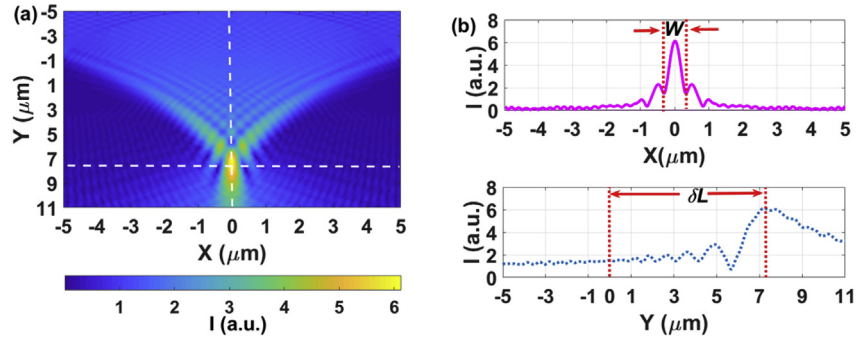


Fig. 2. (a) is the intensity distribution of a TM mode, where $\lambda = 500$ nm and $L1 = 10$ μm and (b) is the intensity distributions along the two white dash lines shown in Fig. (a), where I denotes light intensity and its unit is arbitrary unit, i.e. a.u.

focal spots and will finally be completely absorbed by the bottom perfectly matched layer of our computation area. Fig. 2(a) gives a typical intensity distribution of light refracted by a SCL. In order to quantitatively analyze the properties of a focal spot, we can extract the light intensity distribution of the focal spot along the X and Y directions, as shown by the two white dash lines in Fig. 2(a), where the two lines are parallel to the X or Y axis and pass through the center of the focal spot. Fig. 2(b) is the light intensity distributions extracted from Fig. 2(a) along the two white dash lines, where the values of W and δL are defined as the width of the focal spot in the X direction and the distance between the maximum light intensity point of the focal spot and the bottom surface of the SCL, respectively.

The values of δL and W will determine many geometric parameters of the HE-LTS. Fig. 3 is the variations of the δL and W values with the values of $L1$ and wavelength, where for purpose of comparison, we have

drawn the variations of TE (transverse electric) and TM modes together and except for Fig. 3(b), set the minimum scale values of the horizontal axes at their centers. As shown by Fig. 3(a), the δL values for both TE and TM modes will increase with increasing the $L1$ values at the same wavelength and irregularly fluctuate with increasing the wavelength values for the same $L1$ value. If we use δL_{av} to denote the average value of the δL values at different wavelengths, the variations of the δL_{av} values with the $L1$ values are shown in Fig. 3(b). Due to the $L1$ values larger than the wavelength corresponding to the band gap energy of c-Si material, we can assume that the propagation behavior of light at the interface between the SCL and outside air will strictly obey the law of refraction. The relationships between the values of δL , $L1$ and θ_{inc} can be expressed by,

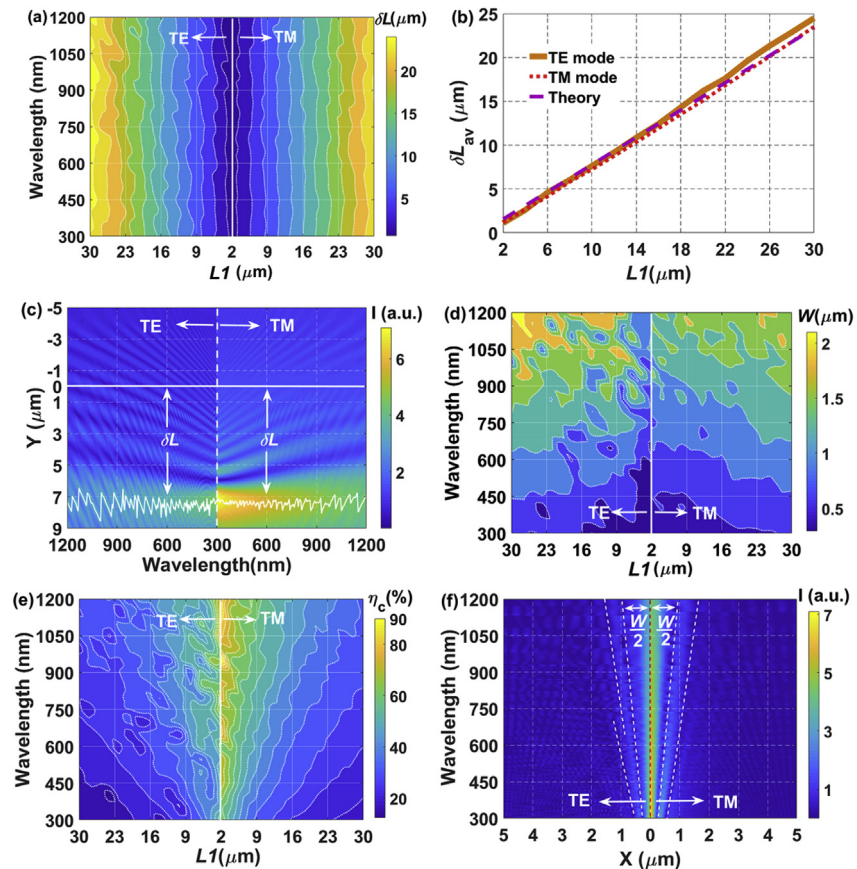


Fig. 3. The variations of the δL and W values with the values of $L1$ and wavelength, where (a) and (b) are corresponding to the δL values; (d) and (e) are corresponding to the W values; (c) and (f) are the variations of the light intensity distributions along the two white dash lines in the X and Y directions, respectively.

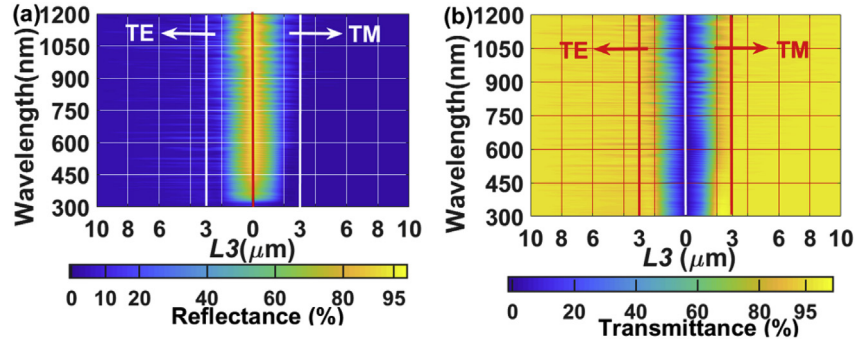


Fig. 4. (a) and (b) are the reflectance and transmittance distributions of the light passing the coupling hole, respectively.

$$\delta L = \frac{L1 \times \sin \theta_{inc}}{2 \tan \left\{ \theta_{inc} - a \sin \left[\frac{n_1}{n_2} \sin(\theta_{inc}) \right] \right\}} - \frac{L1 \times \cos(\theta_{inc})}{2} \quad (2)$$

where n_1 and n_2 are the refractive indexes of air and SiO₂ material, respectively. In Fig. 3(c), the line labeled by “Theory” is calculated by equation (2). As shown by Fig. 3(b), for the same $L1$ values, the δL_{av} values on the “TE mode”, “TM mode” and “Theory” curves are approximately equal to each other in the $L1$ range from 2 μm to 18 μm and exhibit a little bit different in the $L1$ range from 18 μm to 30 μm . With the increase of the $L1$ values, the δL_{av} values on the “TE mode”, “TM mode” and “Theory” curves will increase approximately linearly at a rate of about 0.78 $\mu\text{m}/\mu\text{m}$. Due to the good coincidence between the “TE mode”, “TM mode” and “Theory” curves, equation (2) can be used to predict the δL_{av} values for those larger $L1$ values. In addition, the differences between the δL_{av} values for the “TE mode” and “TM mode” will complicate the design process of the HE-LTS, so the $L1$ values should be selected in the range from 2 μm to 18 μm .

In the following discussion, we will select the values of $L1$ and $H1$ ($=L1/2$) as 10 μm and 5 μm , respectively. The light intensity distributions of different wavelengths along the white dash line in the Y direction (as shown by Fig. 2(a)) is shown in Fig. 3 (c), where $L1 = 10 \mu\text{m}$. As shown by Fig. 3(c), the δL values of different wavelengths for both TE and TM modes are fluctuant in the range from 6 μm to 8 μm . Because the light passing through the focal spot region will spread out in different angles, the minimum δL value of all focal spots for different wavelengths must be located inside the TCMC in order to make incident light completely enter the TCMC. According to Fig. 3(c), we can select the optimal values of $H2$, $H3$ and $H6$ as 5.5 μm , 0.5 μm and 0.5 μm , respectively. The heights of the front and back electrodes, i.e. the values of $H3$ and $H6$, can make light incident on the electrodes totally reflected back into the incident medium.

The variations of the focal spot properties in the X direction are given in Fig. 3(d) and (e). As shown by Fig. 3(d), with the increase of $L1$ and wavelength, the W values are mainly in the range from 0.5 μm to 2 μm ; the larger and smaller W values are mainly distributed in the region with larger $L1$ and wavelength values and in the region with smaller $L1$ and smaller wavelength values, respectively. In order to evaluate the properties of the focal spots along the X direction, we can further defined the concentrating ratio η_c as,

$$\eta_c = \frac{I_W}{I_{L1}} \times 100\% \quad (3)$$

where I_W and I_{L1} denote the integral value of light intensity within the widths of W and $L1$, respectively. As shown by Fig. 3(e), for both TE and TM modes, the η_c values will roughly decrease with increasing the $L1$ values at the same wavelength values. When the $L1$ values are larger, most of the intensity of a focal-spot will distribute outside the regions confined by W . When the $L1$ values are smaller and especially close to $L1 = 2 \mu\text{m}$, most of the intensity of a focal-spot will mainly distribute in the region confined by the W value, but due to the W value approaching

to the corresponding $L1$ value in the longer wavelength range, the focal spots for the longer wavelength will nearly spread over the whole region defined by the $L1$ value.

The light intensity distributions of different wavelengths along the white dash line in the X direction (as shown by Fig. 2(a)) are shown in Fig. 3(f), where $L1 = 10 \mu\text{m}$ and because the light intensity distributions for different wavelengths and for both TE and TM modes are symmetric in the X direction, the range of X values will be chosen from 0 μm to 5 μm for both TE and TM modes. As shown by Fig. 3(f), the regions with the higher light intensity for both TE and TM modes are mainly located in the same range of X values from 0 μm to $W/2 \mu\text{m}$. According to Fig. 3(f), we can see that due to the appearance of the light with weak light intensity outside the region with X values smaller than $W/2 \mu\text{m}$, the $L3$ value cannot be determined only by the W values.

3.2. Optimizing the width of the coupling hole

The coupling hole determines the efficiency of light entering the TCMC. In order to evaluate the efficiency, we replace the c-Si active layer and Ag back electrode in Fig. 1(a) with SiO₂ material, which means that once incident light passes through the coupling hole, it will be completely absorbed by the back perfectly matched layer without any reflection [13]. Fig. 4 (a) and (b) are the reflectance and transmittance of light passing the coupling hole, respectively, where the $L1$, $H1$, $H2$, $H3$ and $H6$ values are chosen as those used in Fig. 3 (c) and (f), i.e. $L1 = 10 \mu\text{m}$, $H1 = 5 \mu\text{m}$, $H2 = 5.5 \mu\text{m}$, $H3 = 0.5 \mu\text{m}$ and $H6 = 0.5 \mu\text{m}$, respectively; the reflectance and transmittance represent the coupling loss and efficiency of light entering the TCMC, respectively. As shown by Fig. 4(a) and (b), the variations of the reflectance and transmittance distributions with the $L3$ and wavelength show opposite trends for both TE and TM modes, i.e. with increasing the $L3$ values, the reflectance and transmittance of light will decrease and increase for the same wavelength value, respectively. The regions with larger reflectance and smaller transmittance are mainly concentrated in the range of $L3$ value from 0 μm to 3 μm . When $L3 \geq 3 \mu\text{m}$, the average reflectance values of the TE and TM modes will be smaller than 8% and 5%, respectively and the average transmittance values of the TE and TM modes will be larger than 92% and 95%, respectively. According to Fig. 4(a) and (b), we will select the optimal value of $L3$ as 3 μm . The optimal value of $L3$ can be further explained by the diffraction orders of the focal spots in Fig. 3(f). In Fig. 3(f), the outer white dash lines, which separate the secondary diffraction orders from other higher diffraction orders, have completely separated the regions with higher light intensities from other regions with very weak light intensities and the maximum X values on these outer white dash lines, which are about 1.5 μm for both TE and TM modes, will determine half of the optimal value of $L3$.

3.3. The coupling efficiency of the TCMC

The light entering the TCMC will be coupled into the ROC by the refraction at the interface between the TCMC and ROC or diffraction

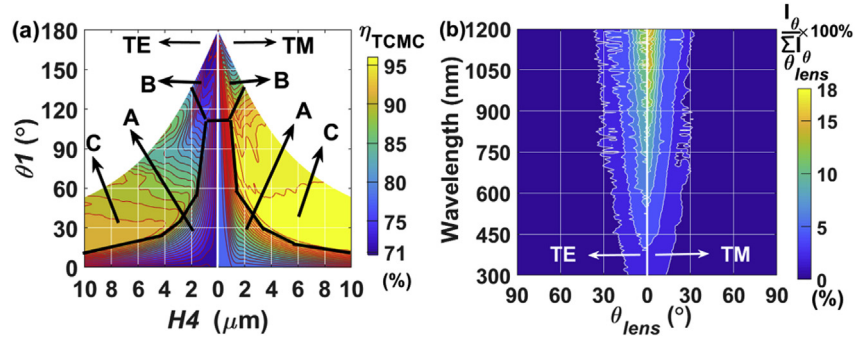


Fig. 5. (a) is the η_{TCMC} values varying with the $H4$ and $\theta1$ values and (b) is the angle-intensity distribution of the light refracted by the SCL.

inside the TCMC. The coupling efficiency of light between the TCMC and ROC (η_{TCMC}) will determine the absorption efficiency of light inside the c-Si active layer and the leakage losses of light from the TCMC to the buffer layer. Here, we can define η_{TCMC} as,

$$\eta_{TCMC} = \frac{J_{T-TCMC}}{J_{T-H}} \times 100\% \quad (4)$$

where J_{T-H} and J_{T-TCMC} denote the photocurrent densities calculated by the transmittances of the light passing through the coupling hole and entering the ROC, respectively. The transmittances of different wavelengths for calculating J_{T-H} can be obtained by Fig. 4(b) (i.e. the transmittances of different wavelengths along the line $L3 = 3 \mu\text{m}$). In order to obtain the transmittances of different wavelengths for calculating J_{T-TCMC} , we will put the bottom perfectly matched layer of our computation region immediately below the bottom boundary of c-Si active layer and set the image part of refractive index of c-Si material to zero. By these settings, the transmittances of the light passing through the TCMC and entering c-Si active layer can be recorded by the record plane setting on the bottom boundary of c-Si active layer.

Fig. 5(a) gives the η_{TCMC} values varying with the $H4$ and $\theta1$ values, where the values of $L1$ ($= 2 \times H1$), $L3$, $H2$, $H3$ and $H6$ are selected as those optimal values obtained in Fig. 3(c) and (f) and Fig. 4 and the value of $H5$ is chosen as $0.5 \mu\text{m}$. From a geometric point of view, the maximum value of $L2$ is equal to the value of $L1$, so some of the larger $\theta1$ values will not exist for a specific nonzero value of $H4$. According to the values of $\theta1$ and $H4$, we can divide the effective regions with different $\theta1$ and $H4$ values into three subregions for both TE and TM modes, i.e. the subregion A, subregion B and subregion C, which have been separated by black solid lines in Fig. 5(a). As shown by Fig. 5(a), the η_{TCMC} values in the subregion C are larger than those in the subregion B and subregion C for both TE and TM modes; the maximum η_{TCMC} values for both TE and TM modes are 91% and 96%, respectively; the η_{TCMC} values for TM modes are larger than those for TE modes at each point ($H4$, $\theta1$) within the three subregions.

The differences between the interaction modes of light with the TCMC, which are determined by the geometric parameters of $\theta1$ and $H4$, are the main reasons why the η_{TCMC} values vary with the values of $H4$ and $\theta1$. When the values of $\theta1$ and $H4$ fall into the subregion A, where the values of $L2$ will be much smaller than those of $L3$, a portion of the light refracted by the SCL will be reflected by the flat upper surface of c-Si active layer and can not enter the ROC by the coupling effects of the TCMC. The smaller the values of $\theta1$ and $H4$ in the subregion A, the smaller the η_{TCMC} values. When the values of $H4$ and $\theta1$ fall into the subregion B, where each wall of the TCMC will tend to be parallel to the flat upper surface of c-Si active layer, the light entering the TCMC will easily escape from TCMC by the reflections of the walls of the TCMC. When the values of $\theta1$ and $H4$ fall into the subregion C, where the values of $L2$ will be close to or larger than those of $L3$, nearly all the light passing through the coupling hole can enter the TCMC, where the obvious refraction and diffraction effects of light will be produced. The differences between the light-reflection losses in the

subregion A, subregion B and subregion C, will make the η_{TCMC} values in the subregion C obviously larger than those in the subregion A and subregion B. Due to the sum of the reflectance and transmittance equal to 1 for a specific wavelength, the losses of η_{TCMC} values caused by the reflection losses are not provided in Fig. 5 for TE and TM modes.

The subregion C can also be further divided into two subregions by the line $\theta1 = 60^\circ$, i.e. the lower and upper subregions. The predominant coupling mechanisms of light for the lower and upper regions are the diffraction and refraction effects, respectively. Fig. 5(b) gives the angle-intensity distributions of the light refracted by the SCL, where we have adopted the same assumptions as those used in Fig. 4 and I_θ denotes the intensity of the light propagating in the θ_{lens} direction. Because the light intensity distributions for different wavelengths are symmetric with respect to the line $X = 0 \mu\text{m}$ (as shown by Fig. 2(a)), Fig. 5(b) only gives the angle-intensity distributions in the θ_{lens} range from 0° to 90° for both TE and TM modes. As shown by Fig. 5(b), the regions with higher light intensity for both TE and TM modes are mainly in the range of $|\theta_{lens}|$ from 0° to 30° . The incident angle (θ_w) of the light entering in TCMC with respect to the walls of the TCMC will obey the following relation,

$$\theta_w = 90^\circ - (2m - 1)\theta1/2 - |\theta_{lens}| \quad (5)$$

where m ($= 1, 2, 3, \dots$) is the reflection number of the light reflected by the walls of the TCMC. When $\theta_w > 0$ and $\theta_w \leq 0$, the light reflected by the walls of the TCMC will propagate towards the bottom and top of the TCMC, respectively. The $\theta1$ angles in the lower and upper region of the subregion C are close to acute and obtuse angle, respectively. In the lower region of the subregion C, the light entering the TCMC can propagate a longer distance toward the bottom of the TCMC by reflected many times ($m > 1$ for a smaller θ_{lens} value) or one time ($m = 1$ for a larger θ_{lens} value) by the walls of TCMC. Because the light in the lower region have the opportunity to be very close the bottom of the TCMC and the height of the region satisfying the diffraction condition is large for the lower region, the strong diffraction effects for all wavelengths will appear at the bottom of the TCMC. In the upper region of the subregion C, a significant fraction of the light entering the TCMC will escape from the TCMC by reflected one time ($m = 1$) by the walls of the TCMC, but due to the reflection effect of the front-surface rectangular electrode, they will be reflected back to the TCMC. By the multi-reflection effects, the light in the upper region will be confined in the TCMC and finally enter the ROC by the multi-refraction effects. Due to the diffraction effects more effective than the refractive effects, the η_{TCMC} values in the lower region are larger than those in the upper region.

3.4. The light trapping efficiency of the ROC

Once light enters the ROC, it will be trapped in the ROC by the reflection effects of the front and back surface electrodes. The photocurrent density (J_{A-ROC}), which is often used to evaluate the light trapping effects of a specific HE-LTS, can be obtained by the

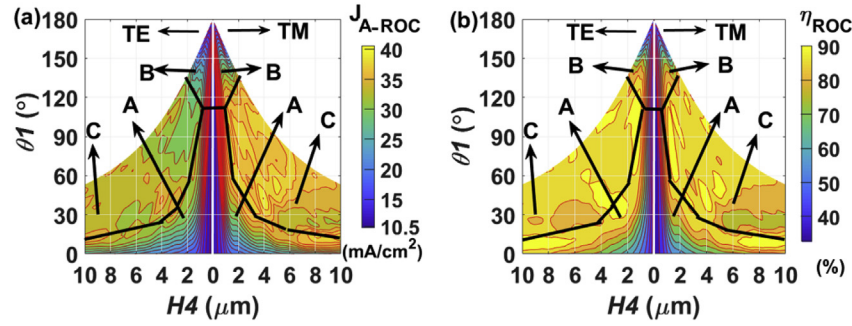


Fig. 6. (a) and (b) are the J_{A-ROC} and η_{ROC} distributions varying with the values of $H4$ and θ_1 , respectively.

absorptance of the light entering the ROC. Due to the geometric parameters of the TCMC determining the propagation properties of the light entering the ROC, they also have important influences on the values of J_{A-ROC} , as shown by Fig. 6(a), where the values of $L1$ ($= 2 \times H1$), $L3$, $H2$, $H3$, $H5$ and $H6$ are selected as those we have used in Fig. 5. In Fig. 6(a), the valid region of the θ_1 and $H4$ values are also divided into three identical subregions as those divided in Fig. 5(a). As shown by Fig. 6(a), the distribution shapes of the J_{A-ROC} values almost have the same shapes as those of the η_{TCMC} values in Fig. 5(a), which indicates that the coupling efficiency of the TCMC will have a key impact on the photocurrent density; the variation trends of the J_{A-ROC} values in these subregions are not quite the same as those of the η_{TCMC} values in the corresponding subregions of Fig. 5(a). Comparing the subregion C in Fig. 6(a) with that in Fig. 5(a), the region boundaries with larger J_{A-ROC} values extends obviously from the subregion C of Fig. 5(a) towards the subregion A and subregion B of Fig. 5(a). The differences in the variation trends of the J_{A-ROC} values and the area variations of the region with larger J_{A-ROC} values can be explained by the variations of the light trapping ability of the ROC with the values of $H4$ and θ_1 . Here, we introduce the concept of the light trapping efficiency (η_{ROC}) to evaluate the light trapping ability of the ROC, as following,

$$\eta_{ROC} = \frac{J_{A-ROC}}{J_{T-TCMC}} \times 100\% \quad (6)$$

where the method for calculating the J_{T-TCMC} value has given in equation (4). Fig. 6(b) gives the distributions of the η_{ROC} values varying with the geometric parameters of $H4$ and θ_1 . As shown by Fig. 6(b), the region with the η_{ROC} values close to 90% appears not only in the subregion C, but also in the subregion A and subregion B; the variation trends of the η_{ROC} values with the values of $H4$ and θ_1 are very different from those of the η_{TCMC} values with the values of $H4$ and θ_1 in Fig. 5(a). Under the combined influence of the variations of the η_{TCMC} and η_{ROC} values with the θ_1 and $H4$ values, the variation trends of the J_{A-ROC} values and the area variations of the region with larger J_{A-ROC} values have different laws from those of η_{TCMC} and η_{ROC} values.

Due to the important influences of the η_{ROC} values on the J_{A-ROC} values, here we will further discuss the light trapping mechanism of the ROC. In fact, the roles of the front and back surface electrodes are similar to those of plane mirrors, so the propagation behaviors of the light in the ROC are mainly determined by the propagation direction of light initially entering the ROC, i.e. the deviation angle of θ_d (as shown in Fig. 1(b)). In order to calculate the θ_d values for different wavelengths, we also adopt the same numerical methods as those used in [Ref.4] and the same assumptions as those used in Fig. 5(a). By these settings, the light initially entering the ROC passes through the c-Si active layer without the absorption and reflection and its propagation direction remains unchanged until it can be completely absorbed by the bottom perfectly matched layer.

Fig. 7 gives the angle-intensity distributions of the light initially entering the c-Si active layer, where the light intensity in a specific θ_d direction for each wavelength has been represented as the percentage

relative to its total light intensity. Because the intensity distribution of each wavelength is symmetric with respect to the line $X = 0$ μm for both TE and TM modes, Fig. 7 only gives the angle-intensity distribution of light in the θ_d range from 0° to 90° . As shown by Fig. 7(a), where the point falls into the subregion B of Fig. 6(a), the θ_d value with higher light intensity mainly concentrates in a small angle range for both TE and TM modes, i.e. $-10^\circ \leq \theta_d \leq 10^\circ$. Due to the walls of the TCMC approximately parallel to the flat upper surface of c-Si active layer and the real part of the complex refractive index of c-Si material larger than that of SiO_2 for each effective absorption wavelength, the angle range with higher light intensity will be compressed from the larger angle range of θ_{lens} in the buffer layer to the smaller angle range of θ_d in the c-Si active layer by the refraction of light at the interface between the SiO_2 and c-Si material. As shown by Fig. 7(b), where the point falls into the subregion A of Fig. 6(a), the θ_d value with higher light intensity mainly concentrates in three angle ranges for both TE and TM modes, i.e. $-15^\circ \leq \theta_d \leq 15^\circ$, $-90^\circ \leq \theta_d \leq -50^\circ$ and $50^\circ \leq \theta_d \leq 90^\circ$, where the first angle range corresponds with the refraction of light at the flat upper surface of c-Si active layer and the last two angle ranges correspond with the stronger diffraction effects of light inside the TCMC. As shown by Fig. 7(c), where the point falls into the subregion C of Fig. 6(a) and is close to the boundary between the subregion A and subregion C, the θ_d value with higher light intensity mainly concentrates in two angle regions for both TE and TM modes, i.e. $-75^\circ \leq \theta_d \leq -50^\circ$ and $50^\circ \leq \theta_d \leq 75^\circ$, where the influence of the flat upper surface of c-Si active layer on the light entering the ROC has almost completely disappeared and the two symmetric angle ranges mainly correspond with the stronger diffraction effects of light inside the TCMC. As shown by Fig. 7(d), where the point is a general point of the subregion C in Fig. 6(a), the θ_d value with higher light intensity mainly concentrates in two angle ranges for both TE and TM modes, i.e. $-90^\circ \leq \theta_d \leq 45^\circ$ and $45^\circ \leq \theta_d \leq 90^\circ$, where the two angle ranges correspond with the stronger diffraction and refraction effects of the light inside the TCMC.

According to Fig. 1(a), Fig. 5(b), Fig. 6(a) and Fig. 7, we can see that due to the structure symmetry of the c-Si SC and the identical propagation mechanism of light passing through the c-Si SC, the J_{A-ROC} and η_{ROC} value variations with $H4$ and θ_1 and the θ_d value variations with wavelengths have similar trends for TE and TM modes; the light entering the ROC by the stronger refraction and diffraction effects will produce the larger values of J_{A-ROC} and η_{ROC} for both TE and TM modes. The maximum J_{A-ROC} values for both TE and TM modes appear at the same region near the point ($H4 = 4$ μm, $\theta_1 = 41^\circ$), as shown by Fig. 6(a). In the following discussion, we will choose the optimal values of $H4$ and θ_1 as $H4 = 4$ μm, $\theta_1 = 41^\circ$ for the HE-LTS.

3.5. The performance contrast between the HE-LTS and lambertian LTS

The photocurrent density contrast of a specific c-Si SC with a LTS (J_{ph}) and with Lambertian LTS (J_l) is often used to assess the performance of the HE-LTS. Here, we assume that the c-Si active layer

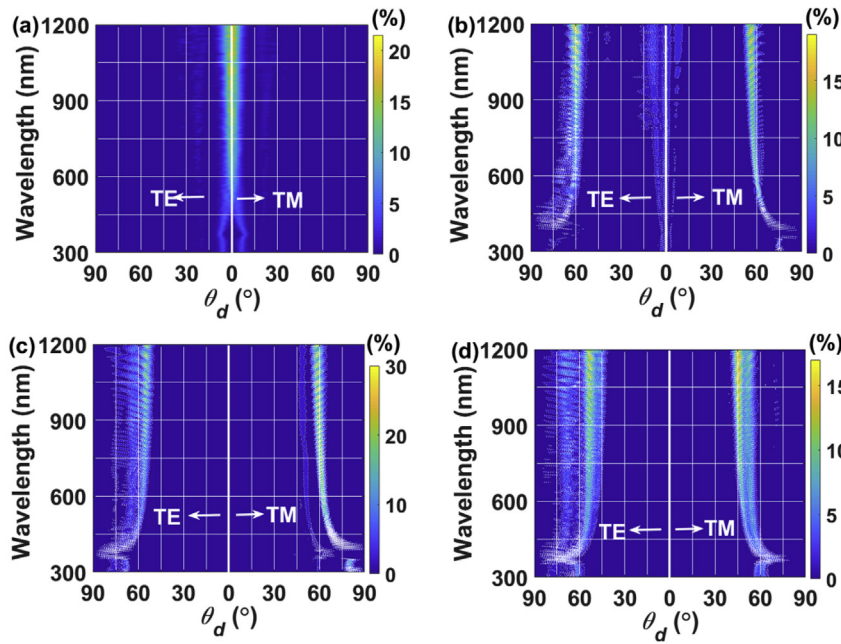


Fig. 7. The angle-intensity distributions of light first entering the c-Si active layer, where (a), (b), (c) and (d) are selected as the points of ($H4 = 1 \mu\text{m}$, $\theta1 = 155^\circ$), ($H4 = 10 \mu\text{m}$, $\theta1 = 5.7^\circ$), ($H4 = 8 \mu\text{m}$, $\theta1 = 14.2^\circ$) and ($H4 = 4 \mu\text{m}$, $\theta1 = 41^\circ$), respectively. The colour bar denotes the percent of light intensity. (For interpretation of the references to colour in this figure legend, the reader is referred to the Web version of this article.)

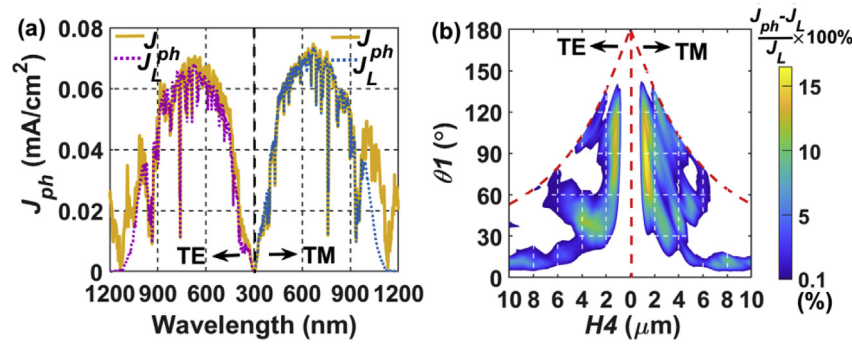


Fig. 8. (a) and (b) are the comparison of the J_{ph} spectra and J_L spectra and the distribution of the J_{ph} values exceeding the corresponding J_L values, respectively.

thickness for Lambertian LTS is equal to $H4$ plus $H5$, as shown by Fig. 1(a) and the reflectance spectrum of the c-Si SC with Lambertian LTS is identical to that with our HE-LTS. The reflectance spectrum of the c-Si SC can be obtained by the relationships between the transmittance and reflectance of Fig. 5(a). Fig. 8(a) shows the comparison of the J_{ph} and J_L spectra, where the geometric parameters of the HE-LTS are selected as their optimal values. In Fig. 8(a), the J_L values for TE and TM modes are 32.39 mA/cm^2 and 36.66 mA/cm^2 , respectively, and the J_{ph} values for TE and TM modes are 36.65 mA/cm^2 and 40.47 mA/cm^2 , respectively. As shown by Fig. 8(a), the J_{ph} values are close to the J_L values in the wavelength range from 300 nm to 970 nm and obviously exceed the J_L values in the wide wavelength range from 970 nm to 1200 nm. Fig. 8(b) gives the distribution of the J_{ph} values exceeding the corresponding J_L values, where the J_{ph} values have been transformed into a percentage form and those points with their J_{ph} values smaller than the corresponding J_L values have been removed. As shown by Fig. 8(b), the region with $J_{ph} \geq J_L$ is in the subregion C of Fig. 6(a) and the maximum J_{ph} value obtained by our HE-LTS can rise by about 16% over that obtained by the corresponding Lambertian LTS for both TE and TM modes.

Fig. 8(b) also shows that the overlapping area between the growth regions for TE and TM modes appears in a wide range of the $\theta1$ and $H4$ values, which will provide a high tolerance to process variations for fabricating the TCMC on the c-Si active layer. According to Fig. 4, Fig5(a) and Fig8(a), the feature sizes of the light trapping unites in the HE-LTS are much larger than the longest wavelength within the

effective absorption wavelength range of c-Si material, so those HE-LTS at the nanoscale can be further added to the HE-LTS to obtain more effective light trapping effects [12]. In addition, due to the values of refractive index of SiO_2 material equal to those of some encapsulating materials of c-Si SCs, such as EVA (ethylene-vinyl acetate) material and glass, the HE-LTS can be uniformly designed with the encapsulating structures of ultrathin c-Si SCs.

4. Conclusion

In this work, we present a new HE-LTS used for ultrathin c-Si SCs and analyze in detail the light trapping mechanisms of the trapping units in the HE-LTS. Some important conclusions can be drawn from our discussion:

- 1) The HE-LTS has an excellent light trapping ability for ultrathin c-Si SCs. The photocurrent density of a ultrathin c-Si SC with the HE-LTS is much larger than that with Lambertian LTS. In actual application, in order to transform the remarkable light trapping ability into the practical performances, the effective surface passivation scheme must be adopted to suppress the serious recombination on the surface of ultrathin c-Si SCs.
- 2) The HE-LTS can improve the filling factor and open circuit voltage parameters of ultrathin c-Si SCs. In fact, if the electrical characteristics (i.e. the dark saturation current density, shunt resistance and diode ideality factor) and ohmic contact properties are identical for

a c-Si SC with the HE-LTS and other HE-LTSs, the filling factor of the c-Si SC with the HE-LTS will be larger than those with other HE-LTSs for the larger area of the front surface electrode and smaller series resistance and the open circuit voltage of the c-Si SC with the HE-LTS will be larger than those with other HE-LTSs for the higher photocurrent density inside the c-Si SC.

- 3) The geometric parameters of the light trapping units of the HE-LTS can vary in a wider range, which means that a larger process error is permitted in fabricating the HE-LTS.
- 4) Although the HE-LTS is designed for ultrathin c-Si SCs, other materials with weaker light absorption coefficients can also obtain a perfect light trapping effect by using the HE-LTS.
- 5) Because the total length of the two walls of the TCMC in the sub-region C is very close to or larger than the length of the corresponding flat c-Si surface and incident light will be absorbed by multiple reflections from the walls of the TCMC, the heat generated in the c-Si SC with our HE-LTS will be kept on the level of the c-Si SC without the convergence of incident light.
- 6) Because incident light must be focused into the TCMC and the propagation direction of incident light must be perpendicular to the front surface, the HE-LTS are well suitable to the concentrating photovoltaic systems, where incident light is always perpendicular to the planes of c-Si photovoltaic modules.

Acknowledgments

This work was supported by program for Natural Science Foundation of Liaoning Province of China (No: 201602008) and National Natural Science Foundation of China (No: 61773074).

Appendix A. Supplementary data

Supplementary data related to this article can be found at <https://doi.org/10.1016/j.solmat.2019.03.036>.

References

- [1] X. Tan, W. Yan, Y. Tu, C. Deng, Small pyramidal textured ultrathin crystalline silicon solar cells with double-layer passivation, *Optic Express* 25 (2017) 14725 <https://doi.org/10.1364/OE.25.014725>.
- [2] S. Manzoor, Z.J. Yu, A. Ali, W. Ali, K.A. Bush, A.F. Palmstrom, S.F. Bent, M.D. McGehee, Z.C. Holman, Improved light management in planar silicon and perovskite solar cells using PDMS scattering layer, *Sol. Energy Mater. Sol. Cell.* 173 (2017) 59–65 <https://doi.org/10.1016/j.solmat.2017.06.020>.
- [3] X. Lu, S. Lun, T. Zhou, M. Zhang, A low-cost high-efficiency crystalline silicon solar cell based on one-dimensional photonic crystal front surface textures, *J. Optics-UK* 15 (2013) 075705 <https://doi.org/10.1088/2040-8978/15/7/075705>.
- [4] X. Lu, P. Zhang, Y. Zhao, Z. Wang, Y. Wu, T. Zhou, H. Lv, Ultrathin crystalline silicon solar cells by textured triangular grating, *Opt. Quant. Electron.* 48 (2016) 50 <https://doi.org/10.1007/s11082-015-0307-y>.
- [5] M.A. Alshal, N.K. Allam, Broadband Absorption enhancement in thin film solar cells using asymmetric double-sided pyramid gratings, *J. Electron. Mater.* 45 (2016) 5685–5694 <https://doi.org/10.1007/s11664-016-4735-7>.
- [6] Z. Xu, H. Huangfu, L. He, J. Wang, D. Yang, J. Guo, H. Wang, Light-trapping properties of the Si inclined nanowire arrays, *Optic Commun.* 382 (2017) 332–336 <https://doi.org/10.1016/j.optcom.2016.08.018>.
- [7] Z. Xu, H. Huangfu, X. Li, H. Qiao, W. Guo, H. Wang, Role of nanocone and nano-hemisphere arrays in improving light trapping of thin film solar cells, *Optic Commun.* 377 (2016) 104–109 <https://doi.org/10.1016/j.optcom.2016.05.050>.
- [8] K.Q. Peng, X. Wang, L. Li, X.L. Wu, S.T. Lee, High-performance silicon nanohole solar cells, *J. Am. Chem. Soc.* 132 (2010) 6872–6873 <https://doi.org/10.1021/ja910082y>.
- [9] S.B. Mallick, M. Agrawal, P. Peumans, Optimal light trapping in ultra-thin photonic crystal crystalline silicon solar cells, *Optic Express* 18 (2010) 5691–5706 <https://doi.org/10.1364/OE.18.005691>.
- [10] M.G. Silveirinha, Trapping light in open plasmonic nanostructures, *Phys. Rev.* 89 (2014) 023813 <https://doi.org/10.1103/PhysRevA.89.023813>.
- [11] R. Sun, H. Fu, J. Wang, Y. Wang, X. Du, H. Zhao, C. Huo, K. Peng, Surface plasmon enhanced light trapping in metal/silicon nanobowl arrays for thin film photovoltaics, *J. Nanomater.* 2017 (2017) 4270794 <https://doi.org/10.1155/2017/4270794>.
- [12] A. Oskooi, Y. Tanaka, S. Noda, Tandem photonic-crystal thin films surpassing Lambertian light-trapping limit over broad bandwidth and angular range, *Appl. Phys. Lett.* 104 (2014) 091121 <https://doi.org/10.1063/1.4867892>.
- [13] X. Lu, X. Wang, J. Gao, Y. Li, Y. Wang, Y. Zhang, Two-cavity light-trapping scheme used in ultrathin c-Si solar cells, *Opt. Lett.* 43 (2018) 4731–4734 <https://doi.org/10.1364/OL.43.004731>.
- [14] I.B. Sohna, H.K. Choia, Y.C. Noha, J. Kimb, M.S. Ahsan, Laser assisted fabrication of micro-lens array and characterization of their beam shaping property, *Appl. Surf. Sci.* 479 (2019) 375–385 <https://doi.org/10.1016/j.apsusc.2019.02.083>.
- [15] P. Nussbaum, R. Volkel, H.P. Herzig, M. Eisner, S. Haselbeck, Design, fabrication and testing of microlens arrays for sensors and microsystems, *J. Opt. A Pure Appl. Opt.* 6 (1997) 617–636 <https://doi.org/10.1088/0963-9659/6/6/004>.
- [16] S. Li, M.M. Jaididi, T.E. Murphy, G. Kumar, Terahertz surface plasmon polaritons on a semiconductor surface structured with periodic V-grooves, *Optic Express* 21 (2013) 7041–7049 <https://doi.org/10.1364/OE.21.007041>.
- [17] X. Lu, X. Wang, J. Gao, Y. Song, Y. Wang, Y. Zhang, The temperature distributions and output parameters of an industrial c-Si solar cell under different environmental conditions, *Sol. Energy* 163 (2018) 84–90 <https://doi.org/10.1016/j.solener.2018.01.068>.
- [18] <https://www2.pvlighthouse.com.au/resources/photovoltaic%20materials/refractive%20index/refractive%20index.aspx>.